Measurement 208 (2023) 112477

Contents lists available at ScienceDirect

Measurement

journal homepage: www.elsevier.com/locate/measurement

Time-Gating method with automatic calibration for accurate measurements of electrically small antenna radiation patterns in Non-Anechoic environments

Adrian Bekasiewicz [a,*], Slawomir Koziel [a,b], Michal Czyz [a]

[a] Faculty of Electronics, Telecommunications and Informatics, Gdansk University of Technology, Narutowicza 11/12, 80-233 Gdansk, Poland
[b] Department of Engineering, Reykjavik University, Menntavegur 1, 101 Reykjavik, Iceland

ARTICLE INFO

Keywords:
Antenna measurement
Calibration
Non-anechoic measurements
Radiation pattern
Small antennas
Time-gating method

ABSTRACT

Non-anechoic sites represent a cheap alternative to measurements of antennas in dedicated facilities. However, due to a high noise—from the external EM signal sources and multipath interferences—the quality of radiation patterns obtained in non-anechoic conditions is poor. The characteristics can be corrected using a time-gating method (TGM), which involves filtering of the noise based on temporal analysis of the measured signals. Unfortunately, determination of appropriate TGM setup is prone to failure due to its manual, or semi-manual nature. In this work, an automatic TGM calibration algorithm for accurate measurements in non-anechoic environments has been proposed. The method involves calibration of the test site using the antenna with known accurate responses. The process is implemented as an optimization routine where TGM intervals are adjusted through a curve fitting of the on-site measurements to the reference radiation patterns. The proposed framework has been demonstrated using four compact radiators and validated against the state-of-the-art techniques. Applicability of the method for calibration of the measurements in distinct test sites, as well as the analysis of the aliasing and external noise on the quality of corrected measurements have also been investigated.

1. Introduction

Prototype measurements belong to the most important steps in the development of microwave components. The goal of the process is to validate accuracy of the simulation models used in the course of the structure development. For antennas, the figures of interest normally include electrical (e.g., reflection, or isolation between the radiators) and/or field (e.g., radiation pattern, or axial ratio) characteristics [1,2]. Although electrical behavior of components can be easily verified using the state-of-the-art equipment such as vector network analyzers (VNA), the field-related responses are normally extracted from a series of measurements performed in anechoic chambers (AC). The latter ones are expensive, specialized facilities that maintain a strictly controlled environment for accurate far-field measurements [3]. ACs are electrically shielded from the external electromagnetic (EM) radiation sources and lined with absorbers that minimize the negative effects of the wall-reflected signals on accuracy of the measured responses. Furthermore, the chambers are equipped with fixtures that ensure appropriate mutual positioning of the antenna under test (AUT) w.r.t. the reference antenna (RA) [3,4].

Due to a high construction cost and large volumes [3], conventional ACs might (and often are) be beyond the reach for budget-constrained research, or teaching activities [39,40]. Alternatively, field performance of antennas can be determined in open-test sites (preferably located in the remote areas, away from the sources of EM radiation and/or objects that could reflect the measured signals) [5,6]. The main challenge associated with open-air measurements involves the negative effects of external factors (i.e., air humidity, wind, etc.) on accuracy and repeatability of the gathered data [3,5,35]. Furthermore, operation of open-test sites often relies on availability of dedicated (hence expensive) permanent facilities (e.g., control rooms, positioning towers), or mobile measurement sets that need to be deployed out of the urban areas (which might be cumbersome and time consuming, when small number of radiators is to be experimentally validated).

The concept of increasing the fidelity of antenna measurements performed in non-anechoic environments has been the subject of intensive research [7–9,16–22]. The most robust techniques reported in the literature are based on the correction scheme that involves (i)

* Corresponding author.
E-mail address: adrian.bekasiewicz@pg.edu.pl (A. Bekasiewicz).

https://doi.org/10.1016/j.measurement.2023.112477
Received 6 November 2022; Received in revised form 13 December 2022; Accepted 10 January 2023
Available online 12 January 2023

measurement of the transmission characteristics between the AUT and the RA over the bandwidth specified around the frequency of interest and (ii) appropriate post-processing (either in the frequency-, or time-domain) of the obtained data oriented towards separation of the signals corresponding to direct transmission on the RA-AUT path from the interferences (mostly in the form of reflections from the walls and/or other obstacles). In [10,16,20], the antenna far-field characteristics have been refined using a matrix-pencil method. The approach boils down to decomposition of the frequency-based measurements into a number of complex exponential functions which represent individual components of the transmission response (i.e., line-of-sight and reflected signals). The identified factors are then averaged to approximate the radiation patterns attainable in the anechoic conditions. Another frequency-based method, is oriented towards extracting the causal far-field responses through numerical optimization of the Chebyshev polynomials [17]. Slightly different approach implements the post-processing based on a time-gating method (TGM) [5,10,22]. In TGM, the measured frequency samples are converted to a time-domain impulse response [10]. The latter is then modified so that the signal components that correspond to the external noise and multipath interferences are suppressed. The corrected impulse responses are then converted back to the frequency-domain so as to facilitate extraction of the radiation patterns.

The discussed methods are predominantly validated in the controlled, semi-anechoic environments, which hinders assessment of their versatility in terms of measurements post-processing in more challenging propagation environments [16–22]. In this regard, TGM may be considered as an exception due to demonstration of its performance in real-world non-anechoic environments [7,9]. In, [7] characterization of the radiator performance figures in a reverberation enclosure (RE) has been proposed. RE is a Faraday cage that provides shielding from the external EM noise but lacks the absorbing materials on the interior walls (required to suppress interferences due to multipath propagation) [8]. In [9], successful characterization of the antenna radiation patterns have been performed in an office room that has not been tailored for far-field measurements in any particular manner except for installation of the antenna positioning fixtures and the VNA.

Despite proved usefulness [5,7,9,10], appropriate setup of TGM—as well as other discussed techniques—for reliable correction of antenna responses is difficult. The performance of the method vastly depends on the bandwidth around the frequency of interest and interval of the time-domain window [7,10]. In the literature, the mentioned factors are determined based on a manual, or semi-manual tuning governed by the rules of thumb [7,9,10]. Although the discussed cognitive approaches proved to be useful, they are also time consuming, prone to failure, and their outcome substantially affects correction performance [11]. Furthermore, the usefulness of TGM—configured w.r.t. a given antenna (also referred to as a calibration structure – CS)—for correcting the responses of other radiators under test has not been scrutinized. Instead, the method is normally validated (through comparisons with AC-based radiation patterns) based on measurements of the same radiator as the one used for setup and often at the same frequency points [9,10]. Moreover, the state-of-the-art TGM approaches exploit excessive number of frequency-points in order to maintain high quality of post-processing which negatively affects the cost of measurements (here, understood as the time required to obtain the data points necessary for reconstruction of the radiation patterns) [7,10,16–21]. Also, the available methods are validated using electrically large, conventional antennas such as rectangular horns, or log-periodic structures [16–21]. Furthermore, usefulness of the method for measurements of compact, planar radiators has not been investigated. From this perspective, the problem concerning application of TGM for low-cost, accurate measurements of electrically small antennas in non-anechoic environments remains open.

In this work, a calibration procedure for automatic determination of TGM correction setup that enables accurate measurements of electrically small antennas in non-anechoic propagation conditions has been proposed. The method involves unsupervised configuration of the test site w.r.t. a calibration structure (CS), i.e., the one for which accurate EM simulations and/or AC-based responses are available. The process is performed using a heuristic algorithm that optimizes interval of the CS impulse responses (obtained through conversion of the frequency measurements to the time-domain) so as to perform a curve fitting of its radiation patterns (extracted from the confined impulse responses restored back to the frequency-domain) to the available reference data. The goal of the calibration is to adjust the properties of the TGM correction to the specific measurement conditions (and class of the antenna under test). Apart from the proposed interval selection algorithm, the novel components of the work include (i) application of the TGM framework for measurements of electrically small antennas, (ii) extraction of reasonably accurate far-field responses at a low cost (time-wise) using small number of data points around the frequency of interest (i.e., the one at which the radiation pattern is to be obtained), and (iii) demonstration of the measurements repeatability when the radiator is characterized in two different test sites. The proposed method has been validated using four example structures: an antipodal Vivaldi radiator, two compact monopoles, and a quasi-Yagi antenna [12–14,31]. The proposed approach has been benchmarked against the methods from the literature in terms of cost and performance. The effects of noise on quality of the TGM-based measurements have also been investigated.

2. Materials

Measurement of antenna characteristics, normally performed in anechoic conditions, is a multi-step process that involves determination of the antenna under test angular location with respect to the reference antenna followed by measurements of transmission between them. Apart from the radiators, the system comprises the positioning devices, signal generator and detector (here, in the form of a VNA), as well as appropriate hardware/software for data acquisition and post-processing. In this section, a brief discussion of these components is provided along with description of the antenna structures used for benchmark of the proposed auto-calibration algorithm.

2.1. Measurement system

A block diagram of the considered system for far-field measurements of antenna characteristics is shown in Fig. 1. Its main components include: (i) positioning towers with control electronics, (ii) VNA, (iii) personal computer, and (iv) connection cables. The towers consist of tripods equipped with the in-house developed rotating heads, which enable 0° to 360° rotation in azimuthal planes of the AUT, and the RA [15]. The measurements are performed using the Anritsu MS2038C vector network analyzer [23]. The system is controlled using a standard personal computer (PC) and the in-house software.

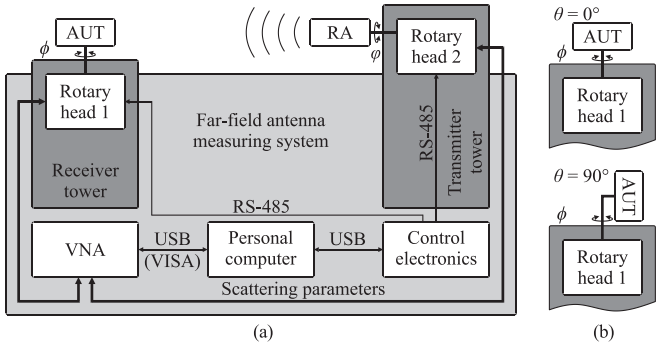

Fig. 1. The considered antenna measurement setup: (a) block diagram of the system and (b) orientations of AUT considered in the work. Thick and thin lines represent the coaxial cables and communication wires, respectively. Parameters ϕ and φ denote angles of AUT and RA, whereas θ represents elevation of AUT.

The above described setup is rather typical for experimental validation of antenna far-field characteristics (apart from the fact that it is not installed in the anechoic chamber) [3,10]. Instead, the equipment is dedicated for use in office rooms that are not tailored to antenna measurements. Here, two test sites are used for experiments in order to demonstrate that the presented post-processing method is capable of generating the radiation patterns characterized by high-resemblance in distinct operational conditions. As shown in Fig. 2(a)-(b), the first test site provides around 2.1 m of line-of-sight distance between the transmitting and receiving antennas (depending on the specific radiators), as well as 1.8 m and 1 m from the towers to the nearest wall and ceiling lamps. It is worth noting that the room is full of equipment (e.g., cabinets, workstations, desks, whiteboard, etc.) that distorts the signals propagated between the antennas and recorded by the VNA. The second site, shown in Fig. 2(c)-(d), is much smaller and hence represents a more challenging testing environment. The positioning towers are separated by around 1.8 m, whereas the shortest distances to the walls are 0.4 m and 0.8 m for the transmitter and receiver tower, respectively. As for the first site, the room is also equipped with computers, bookshelves, whiteboard, electronics, etc. Both offices are adjacent to the main communication passage of the building.

2.2. Antenna structures

Experimental validation of the TGM calibration method presented in this work has been performed using the following (in-house developed) broadband structures: (i) an antipodal Vivaldi radiator based on [12], (ii) a spline-shaped monopole of [13], (iii) a rectangular antenna with trimmed driven element [14], and (iv) a planar quasi-Yagi component with a folded driven element and a rectangular director [31]. Photographs of the manufactured antenna prototypes are shown in Fig. 3. The radiators are equipped with the SMA (SubMiniature version A) connectors from Rosenberger, and Cinch [24,32], respectively. The Vivaldi structure is implemented on a Rogers RO4360G2 dielectric material characterized by a relative permittivity of 6.15 and 0.81 mm thickness [25], whereas both monopoles and the Yagi-based radiator are implemented on a Rogers RO4003C with $\varepsilon_r = 3.38$ and $h = 0.81$ mm [26]. Electrical characteristics of the antennas over the bandwidths considered for experiments are shown in Fig. 4. The responses demonstrate that all of the structures offer low in-band reflection coefficient. It should be emphasized that the far-field radiation patterns of (i) and (ii) have been measured in the anechoic chamber [3,27]. In Section 4, these responses are used for TGM calibration, but also to demonstrate usefulness of the proposed framework for measurements in non-anechoic conditions.

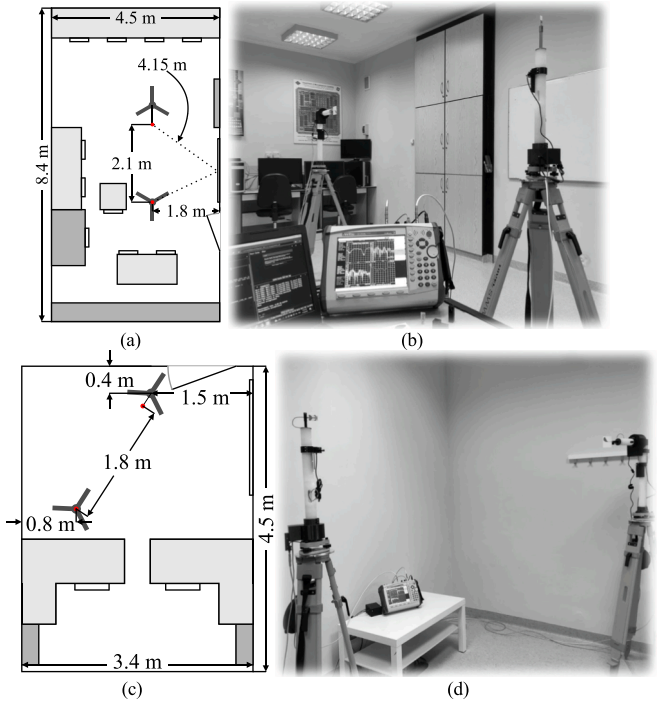

Fig. 2. Measurement sites considered in the work: (a) schematic view and (b) photograph of the first room, as well as (c) view and (d) photograph of the second office. Dotted lines highlight the example path of the reflected signal (the shortest corresponds to reflection from the ceiling lamps), whereas red circles represent the antennas.

3. Methodology

In this section, we formulate the problem pertinent to measurements of the antenna far-field radiation patterns and explain the steps of time-gating algorithm when applied to refinement of the characteristics obtained in non-anechoic environments [7,10]. The challenges related to setup of the method—which provide motivation for development of the proposed calibration mechanism—have also been discussed. Finally, the algorithm for automatic adjustment of the TGM intervals is presented.

3.1. Problem formulation

Let $\boldsymbol{\omega} = [\omega_1 \ \ldots \ \omega_k \ \ldots \ \omega_K]^T$ be the vector of $k = 1, \ldots, K$ frequency points obtained around the center frequency of interest $f_0 = (\omega_1 + \omega_K)/2$. The bandwidth around f_0 is defined as $B = \omega_K - \omega_1$. Then, let

$$\boldsymbol{R} = \boldsymbol{R}(\boldsymbol{\omega}, \boldsymbol{\Phi}) = \begin{bmatrix} R(\omega_1, \phi_1) & \cdots & R(\omega_1, \phi_A) \\ \vdots & \ddots & \vdots \\ R(\omega_K, \phi_1) & \cdots & R(\omega_K, \phi_A) \end{bmatrix} \quad (1)$$

be a set of the measured system responses—i.e., the far-field transmission S_{21} between the RA and the AUT [3]—obtained as a function of $\boldsymbol{\omega}$ and the angular sweep $\boldsymbol{\Phi} = [\phi_1 \ \ldots \ \phi_a \ \ldots \ \phi_A]^T$ ($a = 1, \ldots, A$). For simplicity of notation, only horizontal (azimuthal) angles are considered here, whereas the elevation is set to $\theta = 0$. However, given the hardware capabilities, the analysis can be performed for any combination of θ, ϕ that provide spherical coverage of the AUT characteristics.

The goal of the TGM correction is to create a mapping:

$$g : \boldsymbol{R} \rightarrow \boldsymbol{R}_c \quad (2)$$

where g represents the function that implements time-gating method and $\boldsymbol{R}_c$ is the corrected radiation pattern response of the AUT. The radiation pattern $\boldsymbol{R}_c(f_0, \boldsymbol{\Phi}) = [R_c(f_0, \phi_1) \ \ldots \ R_c(f_0, \phi_A)]^T$ represents the refined antenna measurement obtained at f_0 versus the considered angles of rotation $\boldsymbol{\Phi}$.

3.2. Time-Gating algorithm for Far-Field measurements correction

The TGM correction (2) involves a sequence of steps applied to the measurements performed at all $\boldsymbol{\Phi}$ angles. For the given ϕ_a, the procedure is as follows. First, the frequency-responses are transformed to $\boldsymbol{R}_h(\boldsymbol{\omega}, \phi_a) = \boldsymbol{h}(\boldsymbol{m}_1) \circ \boldsymbol{R}(\boldsymbol{\omega}, \phi_a)$, where "$\circ$" represents component-wise multiplication, $\boldsymbol{m}_1$ is the vector of integers, and $\boldsymbol{h}(\boldsymbol{m}_1)$ denotes cosine-sum function of the following form:

$$\boldsymbol{h}(\boldsymbol{m}) = \alpha_0 - (1 - \alpha_0) \cdot cos(2\pi \boldsymbol{m}) \quad (3)$$

Here, $\boldsymbol{m} = \boldsymbol{m}_1 = [0 \ \ldots \ K-1]^T$ and $\alpha_0 = 0.5$ which corresponds to a Hann window [28]. Fig. 5(a) shows a comparison of $\boldsymbol{R}$ and $\boldsymbol{R}_h$ responses. In the next step, $\boldsymbol{R}_h(\boldsymbol{\omega}, \phi_a)$ is converted to the time-domain using an inverse fast Fourier transform $\boldsymbol{T}(\boldsymbol{t}, \phi_a) = F^{-1}(\boldsymbol{R}_h(\boldsymbol{\omega}, \phi_a), N)$; N represents the number of discrete points used to represent the impulse response [28]. The time-domain sweep is defined as $\boldsymbol{t} = \boldsymbol{n} \bullet \partial t = [t_0 \ \ldots \ t_{N-1}]^T$, where $\boldsymbol{n} = [0 \ \ldots \ N-1]^T$ is the N-point vector of indices and $\partial t = 1/B$ represents the temporal resolution of $\boldsymbol{T}(\boldsymbol{t}, \phi_a)$. Note that ∂t can be determined based on a fractional bandwidth with ω_1 greater than 0 Hz, which leads to non-

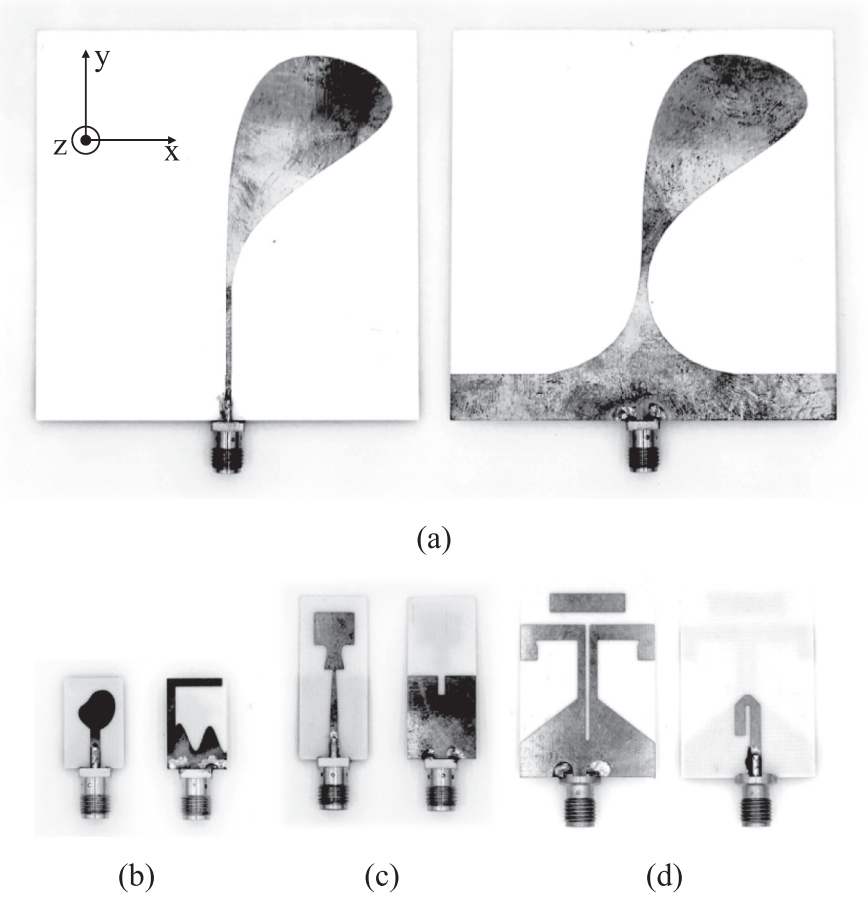

Fig. 3. Photographs (in-scale) of the planar antennas used for demonstration of the presented measurement framework: (a) antipodal Vivaldi [12], (b) spline-based monopole [13], (c) rectangular monopole with trimmed radiator [14], and (d) quasi-Yagi structure [31].

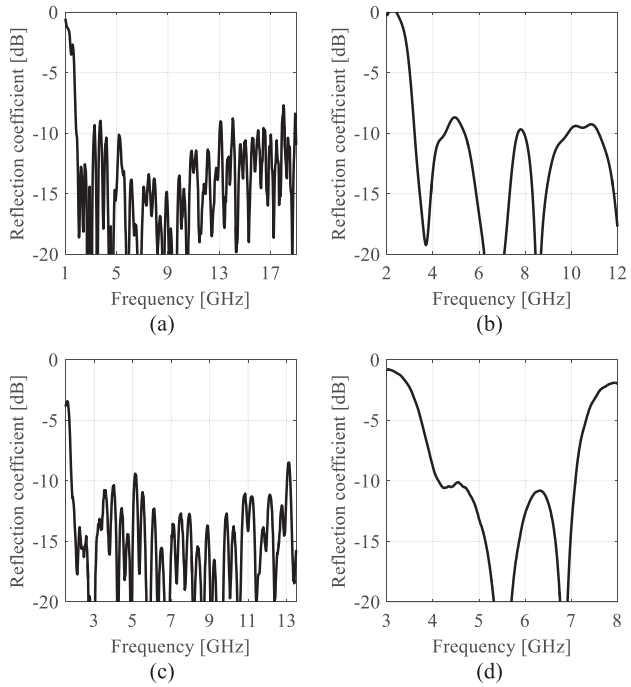

Fig. 4. Reflection coefficients of the considered structures: (a) antipodal Vivaldi [12], (b) spline-based monopole [13], (c) rectangular monopole [14], and (d) quasi-Yagi antenna [31].

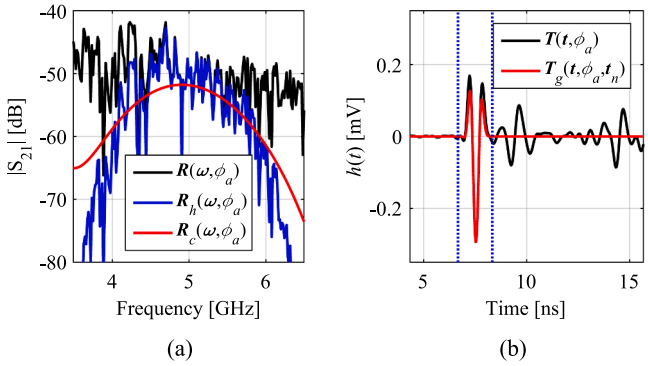

Fig. 5. Visualization of the TGM steps for an example antenna around the center frequency $f_0 = 4$ GHz ($B = 3$ GHz, $\boldsymbol{t}_i = [6.3\ 8.7]$ ns) in: (a) frequency- and (b) time-domain (dotted lines represent bounds of the TGW interval).

causal impulse responses in the time domain (i.e., the ones where $\boldsymbol{T}(t_0, \phi_a)$ is not equal to zero) [29,30]. Notwithstanding, the effect can be neglected due to a relatively large distance between the reference antenna and AUT, as well as preconditioning of the frequency data using (3), which gradually increases attenuation of S_{21} towards edges of the bandwidth (cf. Fig. 5(a)).

The next step involves determination of the gated time-domain response: $\boldsymbol{T}_g(\boldsymbol{t}, \phi_a, \boldsymbol{t}_n) = [0 \bullet \boldsymbol{T}(\boldsymbol{t}_1, \phi_a)\ \boldsymbol{h}(\boldsymbol{m}_2) \circ \boldsymbol{T}(\boldsymbol{t}_{\text{int}}, \phi_a)\ 0 \bullet \boldsymbol{T}(\boldsymbol{t}_2, \phi_a)]^T$, where $\boldsymbol{t}_n = [t_{n1}\ t_{n2}]^T$ represents bounds of the selected discrete interval $\boldsymbol{t}_{\text{int}} = [t_{n1}\ t_{n1+1} \ldots t_{n2-1}\ t_{n2}]^T$ ($t_{n1} < t_{n2} \in \boldsymbol{t}$). The remaining parameters are given as $\boldsymbol{t}_1 = [0 \ldots t_{n1-1}]^T$ and $\boldsymbol{t}_2 = [t_{n2+1} \ldots N]^T$. The vector of integers

for (3) is $\boldsymbol{m}_2 = [0 \ldots n_2 - n_1]^T$, where $n_1 < n_2 \leq N$ are the indices of t_{n1} and t_{n2} (note that the lengths of $\boldsymbol{t}_{\text{int}}$ and $\boldsymbol{m}_2$ are the same). The gated signal $\boldsymbol{T}_g(\boldsymbol{t}, \phi_a, \boldsymbol{t}_n)$ is a composition of a Hann-window-modified fraction of the time-domain response $\boldsymbol{T}(\boldsymbol{t}, \phi_a)$ that corresponds to the $\boldsymbol{t}_{\text{int}}$ interval and zeros for the remaining time steps. A comparison of $\boldsymbol{T}(\boldsymbol{t}, \phi_a)$ and $\boldsymbol{T}_g(\boldsymbol{t}, \phi_a, \boldsymbol{t}_n)$ responses is shown in Fig. 5(b). The gated impulse response is then converted back to the frequency-domain using an N-point fast Fourier transform $\boldsymbol{R}_g(\boldsymbol{\Omega}, \phi_a) = F(\boldsymbol{T}_g(\boldsymbol{t}, \phi_a), N)$ [28], where $\boldsymbol{\Omega} = \boldsymbol{n} \bullet \partial\omega$, $\partial\omega = B/(K-1)$. Note that $\boldsymbol{\Omega}$ is the N-point response whereas $\boldsymbol{\omega}$ is a K-point vector, but $\Omega_{k+1} - \Omega_k = \omega_{k+1} - \omega_k = \partial\omega$. Consequently, the corrected transmission between RA and AUT can be extracted by selecting the first K samples from the $\boldsymbol{R}_g$ response as $\boldsymbol{R}_c(\boldsymbol{\omega}, \phi_a) = [\boldsymbol{R}_g(\Omega_1, \phi_a) \ldots \boldsymbol{R}_g(\Omega_K, \phi_a)]^T$, where $\Omega_1 = \omega_1$ and $\Omega_K = \omega_K$, respectively.

The time-gating algorithm can be summarized as follows:

1. Set $a = 1$;
2. Calculate $\boldsymbol{R}_h(\boldsymbol{\omega}, \phi_a) = \boldsymbol{h}(\boldsymbol{m}) \circ \boldsymbol{R}(\boldsymbol{\omega}, \phi_a)$;
3. Convert $\boldsymbol{R}_h(\boldsymbol{\omega}, \phi_a)$ to time-domain response $\boldsymbol{T}(\boldsymbol{t}, \phi_a)$;
4. Obtain the gated time-domain response $\boldsymbol{T}_g(\boldsymbol{t}, \phi_a, \boldsymbol{t}_n)$;
5. Determine $\boldsymbol{R}_g(\boldsymbol{\Omega}, \phi_a)$ by converting $\boldsymbol{T}_g(\boldsymbol{t}, \phi_a, \boldsymbol{t}_n)$ to the frequency-domain;
6. Extract the corrected response $\boldsymbol{R}_c(\boldsymbol{\omega}, \phi_a)$ from $\boldsymbol{R}_g(\boldsymbol{\Omega}, \phi_a)$;
7. If $a = A$, END; otherwise set $a = a + 1$ and go to 2.

3.3. Appropriate TGM setup – Challenges and mitigation strategies

The performance of TGM varies with the selected B, K, as well as interval of the time-gating window (TGW) represented by the t_{n1} and t_{n2} instances. According to [7,10], the TGM fidelity increases proportionally to bandwidth around f_0. The reasoning here is that increasing B results in improved temporal resolution (i.e., smaller ∂t) between the samples of the impulse response. The effect can be leveraged to determine the interval that is restricted to direct transmission of the signal on the RA-AUT path. The problem of bandwidth determination is often intertwined with (direct, or indirect) analysis of the mentioned interval bounds. Note that, owing to the inverse relation between bandwidth and resolution of the time-domain signal (cf. Section 3.2), enhancement of the former is considered useful for more precise identification of the lower/upper bounds of the interval pertinent to the RA-AUT impulse response.

In [10], the bandwidth is specified as $B \geq 5 \bullet c/(\delta_{n2} - \delta_{n1})$, where δ_{n1} and δ_{n2} denote the (manually measured) line-of-sight RA-AUT distance and the (expected) shortest path travelled by the reflected (e.g., from the ceiling; see Fig. 2) signal; c is the speed of light. Note that, in [10], the bounds of the TGW interval (rectangular window is used instead of Hann) are estimated as $\tau_{n1} = \delta_{n1}/c$ and $\tau_{n2} = \delta_{n2}/c$, respectively. The necessity to measure physical distances in the test site make the approach cumbersome (especially when the test equipment is mobile) and prone to failure. Furthermore, due to the limited spatial–temporal resolution—for TGM, the distance between the towers is represented by a discrete step $\partial d = c \bullet \partial t$—the τ_{n1}, τ_{n2} parameters obtained from site measurements have to be re-set to their discrete counterparts t_{n1}, t_{n2} coinciding with granularity of the data. Unequivocal determination of specific time-instances might not be straightforward (see Fig. 6). Another problem is that the interval bounds determined based on the path travelled by the line-of-sight and the (expected) reflected signals largely depend on the size of the test site. Consequently, it might not confine only the relevant part of the impulse response but also the noise from the external EM sources and other unpredicted interferences (such as reflections from ceiling lamps). Having that in mind, usefulness of the method for post-processing of the measurements performed in unshielded, non-anechoic environments might be limited [9].

A less involving approach to bandwidth estimation has been demonstrated in [7], where $B \geq 3/(t_2 - t_1)$ is suggested to ensure acceptable correction performance, whereas $t_1 = \min(\boldsymbol{t}_{\text{ang}})$ and $t_2 = \max(\boldsymbol{t}_{\text{ang}})$. The vector $\boldsymbol{t}_{\text{ang}} = [t_1 \ldots t_a \ldots t_A]^T$ consists of the time instances pertinent to maximum values of the RA-AUT impulse responses extracted as a function of rotation angles. It is obtained as:

$$t_a = \underset{t_a \in \boldsymbol{t}}{\operatorname{argmax}}(|\boldsymbol{T}(\boldsymbol{t}, \phi_a)|) \tag{4}$$

Compared to [10], the method of [7] does not rely on manual characterization of the test site and enables determination of bandwidth based just on the gathered data. In practical applications, one would perform measurement of $\boldsymbol{R}$ using the arbitrary B in order to extract the impulse responses. Then, appropriate coefficient can be determined through analysis of the obtained characteristics. Due to the symmetry of the time-domain response, the TGW bounds in [7] are estimated as $t_{n1} = -t_2$ and $t_{n2} = t_2$, which corresponds to $t_{n1} = 0$, $t_{n2} = t_2$ when only its non-negative part is considered (as in this work). As an alternative to the approach based on (4), determination of t_{n1} based on a visual inspection of the impulse response has been considered.

As shown in Fig. 7, for practical measurements conducted in non-

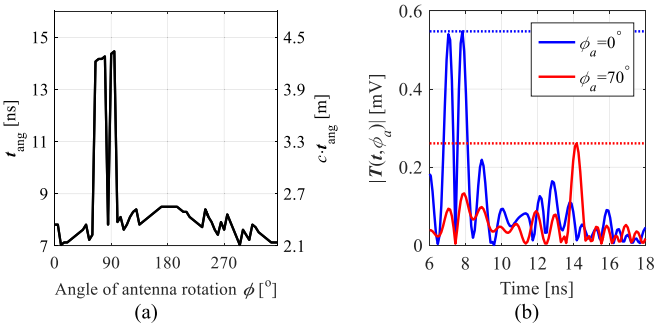

Fig. 7. Time-domain analysis of the impulse response obtained in the first test site for the (directional) Vivaldi antenna (used as AUT) around $f_0 = 6$ GHz frequency with $B = 1$ GHz: (a) transmission delay of the maximum RA-AUT impulse response as a function of antenna rotation, and (b) absolute value of the impulse response for the selected angles of AUT rotation (dotted lines mark the maximum values). Note that, due to low gain of the AUT in the direction of RA at $\phi_a = 70°$, the amplitude of the signal reflected from the whiteboard (see Fig. 1(a)) is larger than the one resulting from the line-of-sight transmission.

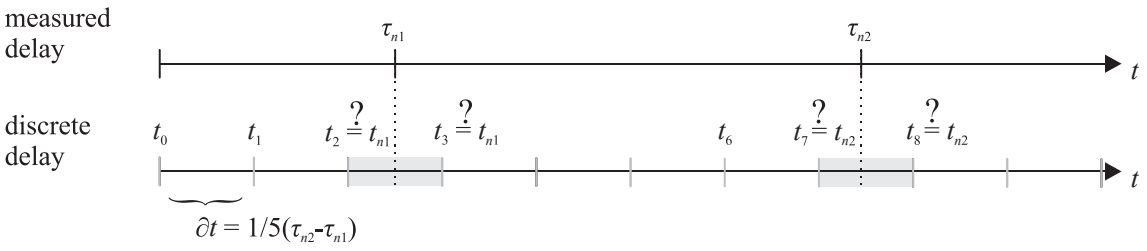

Fig. 6. Manual identification of τ_{n1} and τ_{n2} bounds based on measurements of the line-of-sight RA-AUT distance and the expected shortest path of the reflected signal. Note that, upon determination of ∂t, the granularity of the discrete time-domain steps does not coincide with the measured delays. Consequently, the identification of appropriate t_{n1} and t_{n2} might not be straightforward.

anechoic environments, determination of t_{n1}, t_{n2} from [7] may lead to overestimation of the interval. Although the latter may be acceptable in reverberation chambers, "contamination" of the unshielded environments by the EM signals, might lead to notable degradation of the correction performance. Consequently, the interval should be possibly narrow and centered around the impulse response peak so as to mitigate the effects of propagation conditions on the measurements quality. Another problem is that exaggerated intervals obtained using method [7] result in underestimation of B around f_0, which in turn reduces temporal resolution of the impulse response and negatively affects the correction performance. Unfortunately, mechanisms for automatic determination of short intervals centered around the main peak of the impulse response have not been considered in the literature.

The challenges related to low temporal resolution can be mitigated through realization of measurements in a setup where bandwidth around f_0 is broad (which would also aid identification of t_{n1} and t_{n2} bounds). On the other hand, the method limits the range of usable frequencies at which far-field measurements could be performed. In other words, with a low-cost VNA characterized by frequency range of e.g., 1 GHz to 6 GHz and $B = 4$ GHz, one would restrict characterization of antenna performance to the range of only 3 GHz to 4 GHz. From this perspective, determination of appropriate B to the problem is important to ensure applicability of the correction to various propagation scenarios. For measurement of compact radiators, the bandwidth can be estimated as $B \geq c/(3 \bullet D)$, where D is the AUT aperture (in meters). The reasoning behind bounding B from below using the antenna aperture is that the latter is proportional to gain [33]. The gain of small antennas is normally low which is manifested by the reduced amplitude of the impulse response compared to the external noise. Consequently, extraction of the bounds confining the relevant part of their impulse response is challenging process whereas its precision might noticeably affect the correction performance (cf. Section 3.4). To mitigate the effects of external noise on the quality of measurements, the interval bounds should be narrow and possibly accurate. For small radiators, the latter is ensured by high temporal resolution resulting from the use of the proposed bandwidth estimation formula. The presented threshold on B has been validated based on a series of experiments (cf. Section 4). It should be noted that, for the class of antennas considered in this work, the bandwidth should be greater than 0.5 GHz as lower values deteriorate the correction performance (cf. Fig. 8) [7]. Also, the test site must be large enough so as to enable identification of the impulse response components that correspond to direct transmission and the reflected signals.

In [7], high K (i.e., small $\partial\omega$) is suggested to mitigate the effects of aliasing on the correction performance. As shown in Fig. 8, when the measurements are performed in unshielded environments, the effect of increasing the frequency-points density beyond $K \approx 200$ on the quality of TGM correction seem to quickly deteriorate. The reason is that the improvement of TGW performance due to the reduced aliasing is counteracted by far from optimal propagation conditions (cf. Section 4.5). Also, since the cost of data gathering is proportional to K, a low number of frequency points is desirable from the standpoint of measurements cost. The correction performance can also be improved (to some extent) by augmenting the impulse response using the zero-padding technique ($N > K$) [28]. Numerical experiments conducted in the test sites of Fig. 2 indicate that $N = 2^{\log2(\lceil K \rceil)+3}$ is sufficient to ensure smooth time-domain responses which aid precise identification of the t_{n1}, t_{n2} bounds. Note that variations between the responses in Fig. 8 with K are mostly due to the temporal dynamics of the measurement environment (cf. Section 4.5).

Fig. 9 visualizes the TGM correction performance (w.r.t. the measurements performed in AC) as a function of the t_{n1}, t_{n2} bounds. The responses clearly demonstrate (i) the relation between B and the time-domain resolution, as well as (ii) the narrow (and deep) valleys with steep slopes formed by the low-error intervals. Identification of non– or sub-optimal t_{n1}, t_{n2} bounds significantly affect the performance of non-anechoic measurements compared to the results that can be obtained in dedicated environments. One should reiterate that the specific values of t_{n1}, t_{n2} depend on propagation conditions, i.e., the distance between positioning towers, size of the test site, noise, interferences, etc. From this perspective, precise adjustment of the TGM interval bounds is a challenging problem. In this work, t_{n1}, t_{n2} are determined automatically using the heuristic method proposed in the following section.

3.4. TGM calibration algorithm

The proposed calibration routine enables automatic determination of t_{n1}, t_{n2} so as to maximize the TGM performance in unshielded non-anechoic environments. The main requirement for the proposed heuristic algorithm is availability of a so-called calibration structure, i.e., an antenna that has already been characterized (in terms of the radiation pattern performance) either in AC, or by means of accurate EM simulations. The presented method adjusts the t_{n1}, t_{n2} bounds so as to minimize the discrepancy between the CS responses obtained in the test site w.r.t. the accurate reference data.

The algorithm is sequentially executed at the pre-selected frequencies $\boldsymbol{f}_0 = [f_{0.1} \ldots f_{0.p} \ldots f_{0.P}]^T$, $p = 1, \ldots, P$. The initial bounds $\boldsymbol{t}_{n.p}{}^{(0)} = [t_{n1.p}{}^{(0)}\ t_{n2.p}{}^{(0)}]^T$ are selected based on the vector $\boldsymbol{t}_{\text{ang}.p}$ (note that p refers to the given center frequency of measurements) obtained from (4), where $t_{n1.p}{}^{(0)} = \min(\boldsymbol{t}_{\text{ang}.p})$, $t_{n2.p}{}^{(0)} = \min(\{\max(\boldsymbol{t}_{\text{ang}.p}), t_{\max.p}\})$, and $t_{\max.p} = M(\boldsymbol{t}_{\text{ang}.p}) + (M(\boldsymbol{t}_{\text{ang}.p}) - \min(\boldsymbol{t}_{\text{ang}.p}))$. The latter (note that $M(\bullet)$ represents a median operation) mitigates the effects of signal reflections in

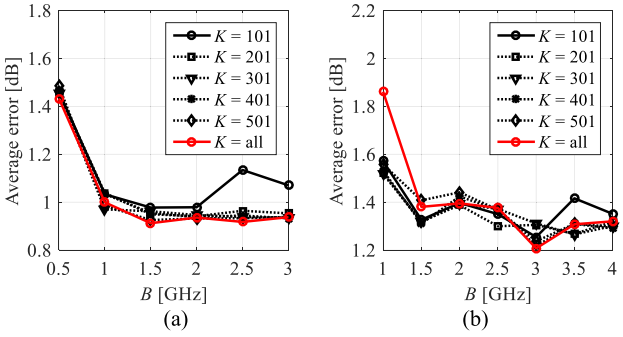

Fig. 8. The effect of B and K on the quality of TGM-based correction expressed in terms of the averaged absolute error w.r.t. AC measurements. The responses are evaluated over $\boldsymbol{f}_0 = [46810]^T$ GHz for: (a) Vivaldi antenna and (b) spline monopole. The parameter K = all denotes that a maximum available number of samples—ranging from ~ 650 (B = 0.5 GHz) to ~ 5350 (B = 4 GHz)—has been used for correction.

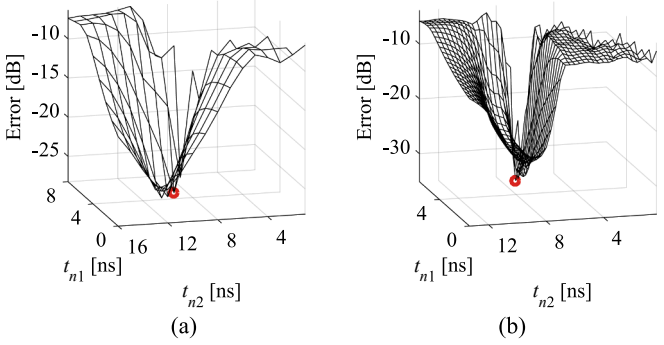

Fig. 9. Measurement error at f_0 = 4 GHz between the results obtained in AC and in the second test site as a function of t_{n1}, t_{n2} bounds: (a) Vivaldi antenna with B = 1 GHz and (b) spline monopole with B = 3 GHz. Note that the bandwidth affects the temporal resolution of the landscapes. Low-error arrangements of t_{n1} and t_{n2} are located in narrow valleys with steep slopes, which hinder their identification.

non-shielded sites on erroneous estimation of the interval (see Fig. 7). In each tuning step $j = 0, 1, \ldots$, the procedure generates perturbed intervals around currently the best design $\boldsymbol{t}_{n.p}^{(j)} = [t_{n1.p}^{(j)}\ t_{n2.p}^{(j)}]^T$ as:

$$\boldsymbol{T}_{n.p}^{(j)} = \begin{bmatrix} \boldsymbol{t}_{-r.-r} & \cdots & \boldsymbol{t}_{-r.0} & \cdots & \boldsymbol{t}_{-r.r} \\ \vdots & \ddots & \vdots & \cdots & \vdots \\ \boldsymbol{t}_{0.-r} & \cdots & \boldsymbol{t}_{0.0} & \cdots & \boldsymbol{t}_{0.r} \\ \vdots & \cdots & \vdots & \ddots & \vdots \\ \boldsymbol{t}_{r.-r} & \cdots & \boldsymbol{t}_{r.0} & \cdots & \boldsymbol{t}_{r.r} \end{bmatrix} \tag{5}$$

where $\boldsymbol{t}_{0.0} = \boldsymbol{t}_{n.p}^{(j)}$. For each pair of integer indices $-r \le m, n \le r$ the perturbed interval is given as $\boldsymbol{t}_{m.n} = [t_{n1.p}^{(j)} + m \bullet \partial t\ t_{n2.p}^{(j)} + n \bullet \partial t]^T$. The candidate solution for the next iteration is selected as:

$$\boldsymbol{t}_{n.p}^{(j+1)} = \arg \min_{\boldsymbol{t}_{m.n} \in \boldsymbol{T}_{n.p}^{(j)}} U(\boldsymbol{t}_{m.n}) \tag{6}$$

The objective function U is of the following form:

$$U = \left\| \boldsymbol{R}_c\left(f_{0.p}, \boldsymbol{\Phi}, \boldsymbol{t}_{n.p}^{(j)}\right) - \boldsymbol{R}_r\left(f_{0.p}, \boldsymbol{\Phi}\right) \right\|_2 \tag{7}$$

Here, $\boldsymbol{R}_r$ is the reference radiation pattern obtained for CS by means of the AC measurements (or the EM simulations). The parameter $\boldsymbol{R}_c(f_{0.p}, \boldsymbol{\Phi}, \boldsymbol{t}_{n.p}^{(j)}) = \boldsymbol{R}_c(f_{0.p}, \boldsymbol{\Phi})$ represents the refined response obtained in non-anechoic environment, where the bounds of the time-gating interval are specified by $\boldsymbol{t}_{n.p}^{(j)}$, i.e., $\boldsymbol{T}_g(\boldsymbol{t}, \phi_a, \boldsymbol{t}_n) = \boldsymbol{T}_g(\boldsymbol{t}, \phi_a, \boldsymbol{t}_{n.p}^{(j)})$, as explained in Section 3.2. The algorithm is terminated when $U(\boldsymbol{t}_{n.p}^{(j+1)}) \ge U(\boldsymbol{t}_{n.p}^{(j)})$ and the final design is selected as $\boldsymbol{t}_{n.p}{}^* = \boldsymbol{t}_{n.p}^{(j)}$. Typically, only a handful of iterations is required for convergence of the method. It is worth noting that the parameter r (the number of TGM evaluations per iteration is $O_{\text{calc}} = (2r + 1)^2$) balances the algorithm cost and performance. The reason is that r controls the range of objective function evaluations around the $\boldsymbol{t}_{n.p}^{(j)}$ design. Here, $r = 2$—which corresponds to span of five samples around $\boldsymbol{t}_{n.p}^{(j)}$ in each direction—is selected as it ensures low tuning cost and mitigates the risk of getting stuck in close-to-optimal, yet not the best available design.

The above described routine is executed sequentially for all P selected frequencies. The resulting bounds of the TGW interval (considered accurate for a range of frequencies) are then obtained as a superposition $\boldsymbol{t}_n^* = [t_{n1}^* t_{n2}^*] = [\lfloor < [t_{n1.1}^* \ldots t_{n1.P}^*] > \rfloor, \lceil < [t_{n2.1}^* \ldots t_{n2.P}^*] > \rceil]$. Note that $<\bullet>$ represents an average, whereas $\lfloor \cdot \rfloor$ and $\lceil \cdot \rceil$ denote round down and up to the nearest discrete multiple of ∂t (cf. Fig. 6). It is worth noting that the algorithm requires at least one reference frequency for calibration of the test site. Increasing P can mitigate the effects of frequency-dependent propagation conditions on the performance of TGM-corrected radiation patterns.

The presented algorithm can be summarized as follows (see Fig. 10 for conceptual illustration of the routine operation):

1. Set $p = 0$, $j = 0$;
2. Find $\boldsymbol{t}_{n.p}^{(j)}$;
3. Generate the interval bounds $\boldsymbol{T}_{n.p}^{(j)}$ around $\boldsymbol{t}_{n.p}^{(j)}$;
4. Obtain $\boldsymbol{t}_{n.p}^{(j+1)}$ by solving (6) using the objective function (7);
5. If $U(\boldsymbol{t}_{n.p}^{(j+1)}) < U(\boldsymbol{t}_{n.p}^{(j)})$, set $j = j + 1$ and go to 3; otherwise set $\boldsymbol{t}_{n.p}{}^* = \boldsymbol{t}_{n.p}^{(j)}$ and go to 6;
6. If $p < P$ set $p = p + 1$ and go to 2; otherwise extract $\boldsymbol{t}_n{}^* = [t_{n1}{}^*\ t_{n2}{}^*]$ and END.

4. Results and discussion

Performance of the proposed TGM-correction framework has been demonstrated in two unshielded non-anechoic measurement sites using a total of four antennas (see Section 2). All measurements have been performed with $K = 201$. It should be noted that the antipodal Vivaldi structure of Fig. 3(a) has been used as the RA (cf. Fig. 1) for all of the considered experiments. The average discrepancies between the reference and TGM-corrected measurements have been expressed in terms of the root-mean-square-error (RMSE):

$$e_R = \frac{1}{\sqrt{A}} \sqrt{\sum_{j=1}^{N} \left(\boldsymbol{R}_c(f_0, \boldsymbol{\Phi}) - \boldsymbol{R}_r(f_0, \boldsymbol{\Phi})\right)^2} \tag{8}$$

The metric (8) has been selected because it finds application in the reference literature [7]. It is worth noting, however, that measurements accuracy can be also expressed in the form of, e.g., equivalent stray signal [34]. The proposed calibration algorithm has been validated against the methods from the literature in terms of the cost and accuracy. The section has been summarized by the discussion of the results with focus on the effects of external noise on performance of the presented framework.

4.1. Antipodal Vivaldi antenna

The experiment involves application of a Vivaldi antenna for calibration of the first test site, w.r.t. the EM simulation data. The identified bounds of the impulse response interval are then re-used for measurement of the same antenna at other frequencies ($\theta = 90°$). The radiator aperture is $D \approx 0.10$ m, hence $B = 1$ GHz has been selected (cf. Section 3.3). The structure has been measured in the yz-plane (see Fig. 3(a)). In the first step, a series of non-anechoic measurements has been performed around the center frequencies of 3 GHz, 4 GHz, 5 GHz, and 8 GHz, respectively. Next, the algorithm of Section 3.4 has been used to perform calibration at $\boldsymbol{f}_{0.\text{cal}} = [3\ 8]^T$ GHz. The resulting vector of interval bounds $\boldsymbol{t}_n{}^* = [5\ 12]^T$ ns (which corresponds to seven samples in the time-domain) has been then used to correct the radiation patterns obtained at $\boldsymbol{f}_{0.\text{eval}} = [4\ 5]^T$ GHz. Fig. 11 shows a comparison of the AC

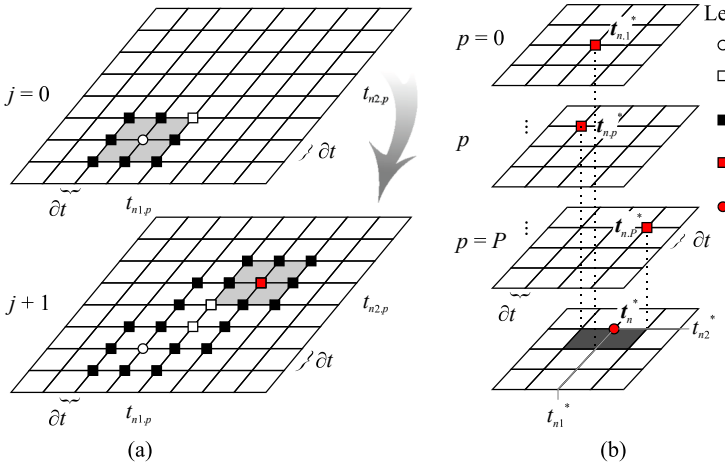

Fig. 10. Conceptual illustration of the proposed TGM bounds optimization algorithm: (a) iterative adjustment of the bounds at pth frequency (with $r = 1$) based on comparison of the radiation pattern obtained for the CS in the non-anechoic test site to the reference one (AC-, or EM-based), as well as (b) extraction of the $\boldsymbol{t}_n{}^*$ bounds based on superposition of the results from $f_{0.p}$ frequencies. The light gray cells in (a) represent the span of $\boldsymbol{T}_{n.p}^{(j)}$ around $\boldsymbol{t}_{n.p}^{(j)}$. The dark gray cells in (b) represent the range determined by $\boldsymbol{t}_{n.p}{}^*$ bounds.

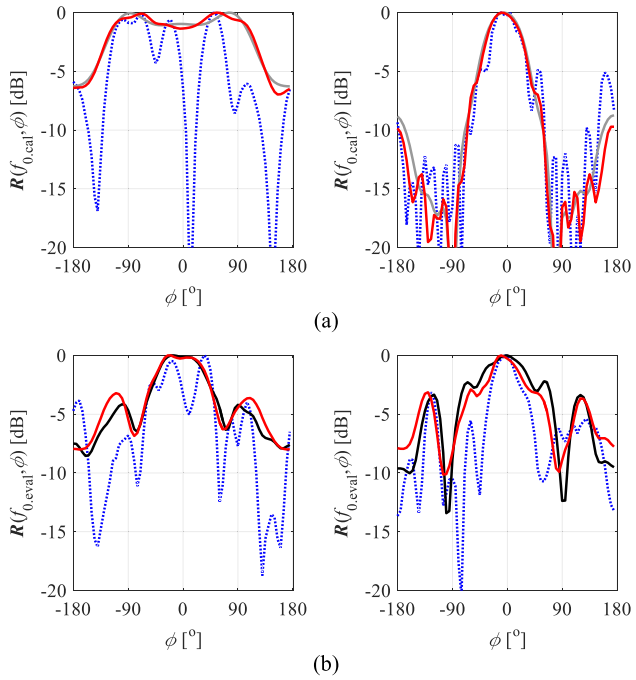

Fig. 11. Corrected (red), reference, and uncorrected (blue) radiation patterns obtained for the Vivaldi antenna measured in yz-plane [12]. The TGM has been calibrated w.r.t. EM simulations (gray) at: (a) $\boldsymbol{f}_{0.\mathrm{cal}} = [3\ 8]^T$ GHz frequencies. The correction has been validated w.r.t. AC measurements (black) at (b): $\boldsymbol{f}_{0.\mathrm{eval}} = [4\ 5]^T$ GHz. Note that uncorrected characteristics feature a substantial discrepancy w.r.t. AC measurements and EM simulations. (For interpretation of the references to colour in this figure legend, the reader is referred to the web version of this article.)

measurements with the obtained results (before and after TGM correction). The average discrepancy between the AC and TGM-based characteristics—expressed using RMSE averaged over the number of considered $\boldsymbol{f}_{0.\mathrm{eval}}$ frequencies—amounts to only –22 dB, which represents over 8.4 dB improvement compared to uncorrected measurements. It is worth emphasizing that, although the discrepancy between the AC and TGM-based responses is noticeable, the measurements have been performed in a unshielded, non-anechoic environment contaminated by the external EM noise. Consequently, the agreement between the responses is acceptable.

The effect of selected interval bounds on TGM correction performance can be demonstrated using a power-angle-delay profile (PADP), which represents the measured impulse response of the AUT as a function of the S_{21} transmission time-delay and angular position of AUT w.r.t. the RA [36,37]. The time domain characteristics obtained in non-anechoic conditions before (with RMSE at 5 GHz of –13 dB), as well as after correction performed using the proposed method, approaches of [10,7], and through manual tuning of the interval are shown in Fig. 12. Comparison of the AC measurements with the refined responses (obtained at 4 GHz and 5 GHz frequencies for $K = 201$ and $B = 1$ GHz) is shown in Fig. 13. The results demonstrate that the effects of considered correction mechanisms on the time-domain responses are mostly subtle. At the same time, the RMSE values obtained at 5 GHz frequency for the presented, and benchmark methods amount to –19.7 dB, –17.9 dB, –18.8, and –16.4, respectively. It should be reiterated that the approach of [10] requires a careful examination of the shortest path for the reflected signal (see Fig. 2), whereas the interval determined using the technique [7] is prone to interference-induced errors (see Fig. 7). Finally, the bounds identified based on visual inspection of characteristics are too aggressive which is manifested through excessive attenuation of the side lobes. Also, for the considered test case, manual tuning is characterized by the smallest improvement of the performance among the compared techniques.

4.2. Compact monopole antennas

The second experiment involves calibration of the first test site using a spline-based monopole antenna shown in Fig. 3(b) w.r.t. the AC-based responses. The identified interval bounds are then used to perform TGM-corrected measurements of the radiator of Fig. 3(c) [14]. The antenna

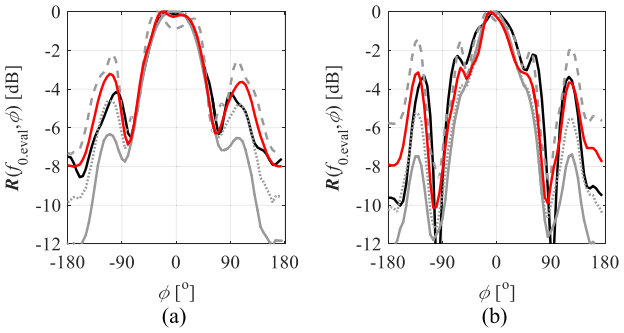

Fig. 13. Antipodal Vivaldi antenna: comparison of the radiation patterns obtained in AC (black), and non-AC conditions using the proposed method (red), as well as the approaches of [10] (– –), [7] (●●●), and obtained through manual adjustment intervals (—). The center frequencies are: (a) 4 GHz and (b) 5 GHz, respectively. Note that excessive trimming of the impulse response for the manually determined interval results in attenuation of the side-lobes. (For interpretation of the references to colour in this figure legend, the reader is referred to the web version of this article.)

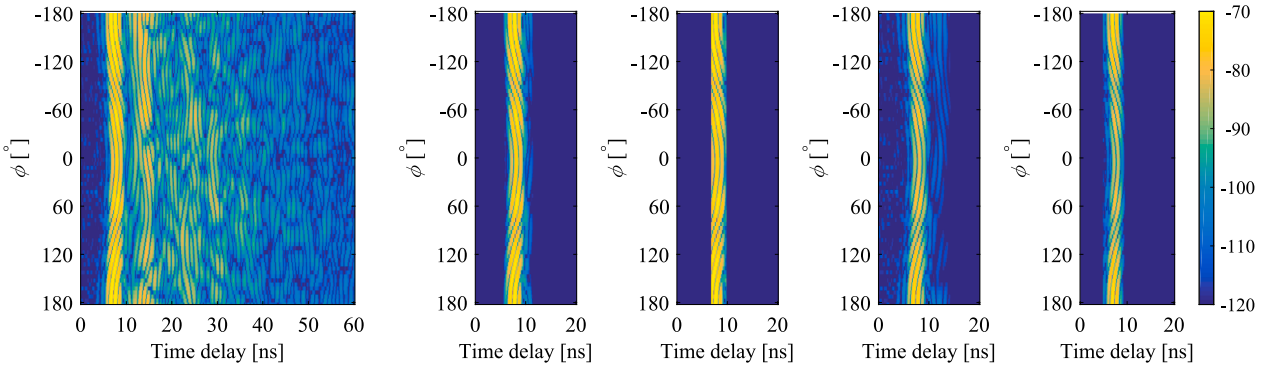

Fig. 12. Vivaldi antenna: PADP obtained in the first test site at 5 GHz frequency for (from left) uncorrected responses and characteristics modified using (from left) the proposed method, as well as the techniques of [10,7], and through manual adjustment of interval bounds. Note that the interval bounds at 4 GHz are the same as the ones used at 5 GHz.

aperture is estimated as $D \approx 0.03$ m, which corresponds to $B = 3$ GHz. Both structures have been measured in xz-plane ($\theta = 0°$). The non-anechoic data have been obtained at $\boldsymbol{f}_{0.\mathrm{cal}} = [4\ 6\ 8]^T$ GHz frequencies. The interval bounds of $t_{n1}{}^* = 6$ ns and $t_{n2}{}^* = 8.7$ ns (which corresponds to eight time-domain samples) have been determined using the algorithm of Section 3.4. As shown in Fig. 14(a), the agreement between the AC and TGW-corrected results at $\boldsymbol{f}_{0.\mathrm{cal}}$ is excellent. The resulting average RMSE is only –30 dB.

The obtained calibration data have been used for TGM correction of the compact monopole from Fig. 3(c), which features aperture with comparable size to the CS (i.e., the radiator of Fig. 3(b)). The considered vector of center frequencies is $\boldsymbol{f}_{0.\mathrm{eval}} = [3\ 12]^T$ GHz. A comparison of the TGM-corrected measurements with the EM simulation results obtained for the considered radiator is shown in Fig. 14(b). The agreement between the characteristics is excellent, especially having in mind that the correction has been performed using different structure and at the frequencies that exceed the range used for calibration. The average RMSE between the EM simulations and corrected measurements is only –28 dB. Note that, for both considered antennas, the uncorrected responses are vastly incorrect.

For the sake of comparison, refinement of the non-anechoic radiation patterns obtained for the antennas of Fig. 3(b)-(c) using methods of [7] and [10] has also been considered. Unfortunately, the benchmark approaches do not improve the characteristics w.r.t. non-corrected responses. In both cases, poor results stem from overestimation of the intervals, as well as due to the fact that they are not centered around the peak of the impulse response coinciding with direct RA-AUT transmission.

Fig. 15 shows the gated responses obtained for the antenna of Fig. 3 (b) using the proposed approach, as well as the methods of [7] and [10]. The results indicate that, for the considered test cases, the benchmark methods offer little-to-no improvement of the RMSE and thus manual tuning of intervals is required. It is worth noting that overestimation of the reflected signal path for the technique of [10] stems from the difficulties in accurate determination of the appropriate location at/near the antenna from which the distance measurements should be undertaken. The same problem is pertinent to both unequivocal estimation of the reflection plane for the signal w.r.t. the geometrically complex structures (here, ceiling lamps – see Fig. 2), or human errors, i.e., identification of a whiteboard instead of the ceiling as the obstacle determining the shortest path of the interferences. For the method of [7], substantially off-centered location of the Hann window w.r.t. the significant part of the impulse response results in its substantial attenuation and hence negligible improvement of corrected radiation pattern w.r.t. the uncorrected one.

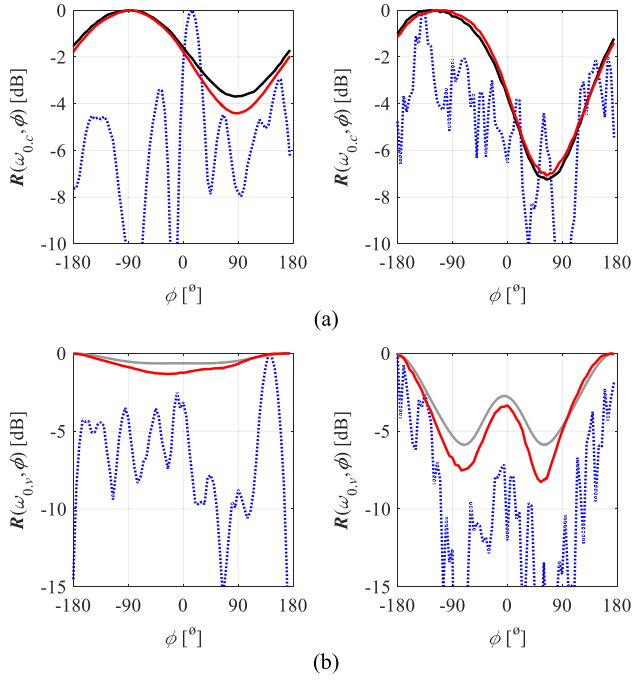

Fig. 14. Corrected (red), reference, and uncorrected (blue) patterns obtained for the spline-monopole antenna of [13] calibrated w.r.t. AC measurements (black): (a) patterns at $\boldsymbol{f}_{0.\mathrm{cal}} = [4\ 7]^T$ GHz ($\boldsymbol{f}_{0.\mathrm{cal}} = 6$ GHz not shown). The correction has been validated w.r.t. EM simulations (gray) using radiator of [14] at (b): $\boldsymbol{f}_{0.\mathrm{eval}} = [3\ 1\ 2]$T GHz. (For interpretation of the references to colour in this figure legend, the reader is referred to the web version of this article.)

A more in-depth insight into the effect of selected TGM intervals on correction performance can be gained using the PADP. Fig. 16 shows the metric obtained for both the calibration antenna and the structure under test before, as well as after the calibration performed using the methods considered above and based on manual tuning of the intervals. Examination of the uncorrected time-domain data indicate that the main peak of the impulse response is very narrow for all of the considered angles of AUT rotation. The signal is followed by interferences with a relatively high-amplitude (compared to the main pulse). Characteristics further support the claim that determination of a narrow time-gating interval centered around the line-of-sight component of the signal is crucial for successful calibration of the test site. For the considered techniques, the uncorrected response of CA (with RMSE of –9.4 dB at 4 GHz) has been refined to, –30.3 dB, –10.7 dB, –13.4 dB, and –24.9 dB, respectively. Regardless of aggressive manual trimming of the interval, the presented method still offers over 2 dB lower correction error, which is due to more rigorous (and multi-frequency-based; cf. Section 3.4) analysis of the responses. The far-field characteristics of CA that correspond to calibration responses (obtained at 4 GHz and 7 GHz) are shown in Fig. 17. The results demonstrate that components of the time-domain data adjacent to the direct impulse response substantially contribute to distortion of the radiation patterns.

4.3. Quasi-Yagi structure

The next case study concerns calibration of the second test site using the Vivaldi antenna (CA) and its AC-based reference responses. The resulting TGM interval has been re-used for measurements of the quasi-Yagi structure of Fig. 3(d) in the yz- and xy-planes ($\theta = 90°$) [31]. The estimated antenna aperture and bandwidth are $D \approx 0.05$ m and $B = 2$ GHz, respectively. The TGM bounds $\boldsymbol{t}_n{}^* = [5.5\ 7.5]^T$ ns have been obtained through automatic calibration at $f_{0.\mathrm{cal}} = 3$ GHz frequency. The RMSE of the gated radiation pattern w.r.t. AC measurements is only –27.5 dB, which represents over 16.5 dB improvement compared to the uncorrected response.

The obtained interval bounds have been used for correction of quasi-Yagi characteristics at $f_{0.\mathrm{eval}} = [4\ 7]^T$ GHz frequencies. Comparisons of the TGM-based responses with the EM simulations are shown in Fig. 18. For the first and second pair of measurements the averaged RMSE values are –23.9 dB and –26.1 dB which represents almost 10 dB and over 15 dB improvement compared to the uncorrected responses.

4.4. Comparison of the measurements from two different test sites

The last considered test case involves comparison of the TGM-corrected radiation patterns obtained in both test sites of Fig. 2. The experiments have been performed using two antennas, i.e., the antipodal Vivaldi and the spline-based monopole. The same calibration/measurement steps have been performed for both structures in both test sites.

For the Vivaldi antenna, the test sites have been calibrated w.r.t. the EM simulation results ($B = 1$ GHz, $\theta = 90°$, yz-plane) at $\boldsymbol{f}_{0.\mathrm{cal}} = [3\ 8]^T$ GHz. The TGM intervals of $\boldsymbol{t}_{n.1}{}^* = [5\ 12]^T$ ns, and $\boldsymbol{t}_{n.2}{}^* = [4\ 10]^T$ ns have been identified in the first and the second test site using the algorithm of

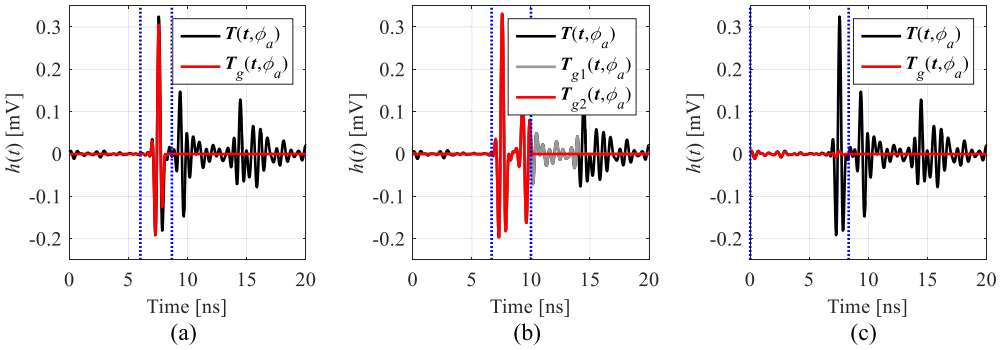

Fig. 15. Impulse response of the spline-based monopole antenna obtained at 4 GHz and $\phi_a = 0°$ with highlight on the time-domain interval (dotted lines) identified using: (a) the proposed algorithm, as well as the methods of: (b) [10] where the shortest path of the reflected signal is determined w.r.t. the whiteboard (gray) and ceiling lamps (red); see Fig. 2, as well as (c) [7], respectively. Note that the benchmark techniques not only overestimate the bounds, but also produce the intervals that are off-centered the impulse response peak. (For interpretation of the references to colour in this figure legend, the reader is referred to the web version of this article.)

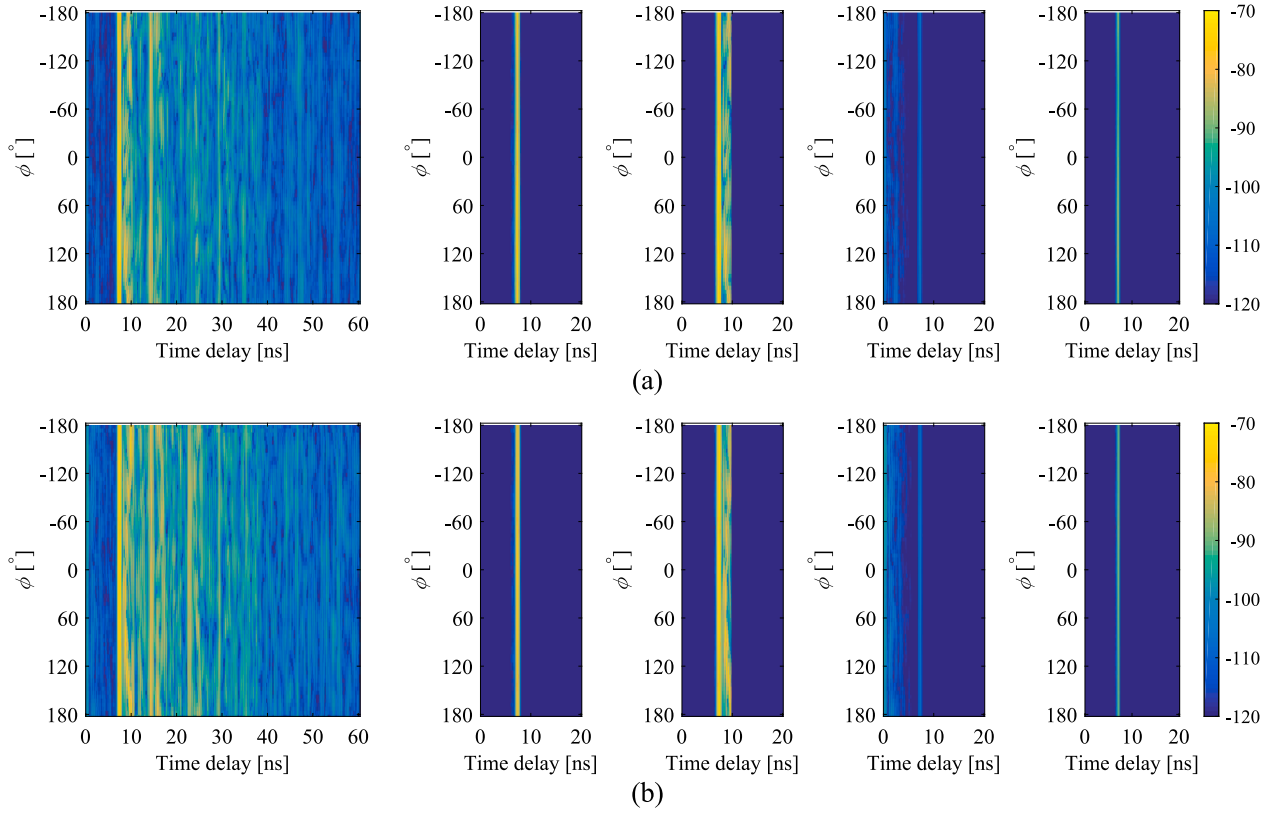

Fig. 16. PADP in the first test site for (from left) uncorrected responses, as well as characteristics modified by the proposed method, the techniques of [10,7], and through manual adjustment of interval bounds. The responses have been obtained using: (a) calibration antenna (spline monopole) at 4 GHz, (b) antenna under test at 3 GHz. Note that high resemblance between PADP for both structures facilitates utilization of the calibration data for accurate correction of the responses.

Section 3.4. Note that the optimized intervals are not the same which stems from different propagation conditions in the rooms. The extracted setup parameters have been utilized for correction of the Vivaldi antenna measurements performed at $f_{0.eval} = [4\ 5]^T$ GHz. Comparisons of the TGM-corrected responses obtained in both test sites against the AC-measurements are shown in Fig. 19. The averaged post-correction RMSE values are –22 dB and –24.5 dB for the first and the second test site, which corresponds to almost 8.5 dB and over 13 dB improvement w.r.t. the uncorrected responses. Furthermore the resemblance between the refined characteristics from both office rooms is relatively high, especially having in mind substantially different propagation conditions.

The monopole antenna has also been calibrated w.r.t. the EM simulation results ($B = 3$ GHz, $\theta = 0°$, xz-plane). The calibration has been performed at $\boldsymbol{f}_{0.cal} = [6\ 9]^T$ GHz and the intervals of $\boldsymbol{t}_{n.1}{}^* = [6.7\ 8.3]^T$ ns, and $\boldsymbol{t}_{n.2}{}^* = [6\ 7]^T$ ns have been found. Then, the TGM-corrected measurements have been obtained at $\boldsymbol{f}_{0.eval} = [4\ 7]^T$ GHz. Fig. 20 shows comparison of the refined non-anechoic measurements with the AC-based radiation patterns. The corrected responses are characterized by RMSE of –28 dB (first site) and –27 dB (second site). The obtained values represent 15.5 dB and 16 dB improvement w.r.t. the non-anechoic data.

Performance of the TGM correction in both test sites is summarized in Table 1. The results clearly indicate that, for the considered test cases, the presented approach substantially improves the quality of measurements performed in unshielded non-anechoic conditions. Furthermore, the characteristics and quantitative information obtained based on the tests demonstrate usefulness of the proposed calibration algorithm for maintaining similar performance of measurements conducted in environments characterized by substantially different propagation properties. The latter seems important not only for obtaining high-quality responses (bearing the far-from-ideal conditions), but also to enable

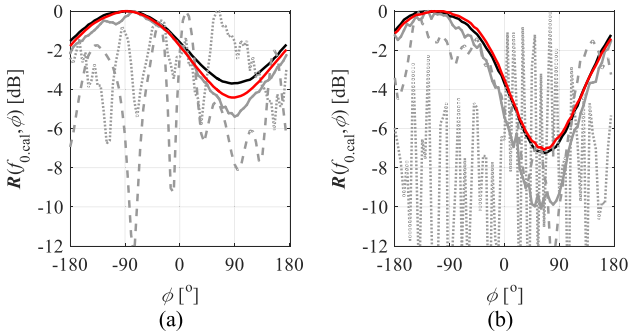

Fig. 17. Calibration of the first test-site using the spline-based monopole: comparison of the radiation patterns obtained in AC (black), and non-AC conditions using the proposed method (red), as well as the approaches of [10] (– –), [7] (●●●), and determined through manual adjustment intervals (—). The center frequencies are: (a) 4 GHz and (b) 7 GHz, respectively. Note that the methods [7] and [10] are useless for calibration of the test site to the considered compact radiator. (For interpretation of the references to colour in this figure legend, the reader is referred to the web version of this article.)

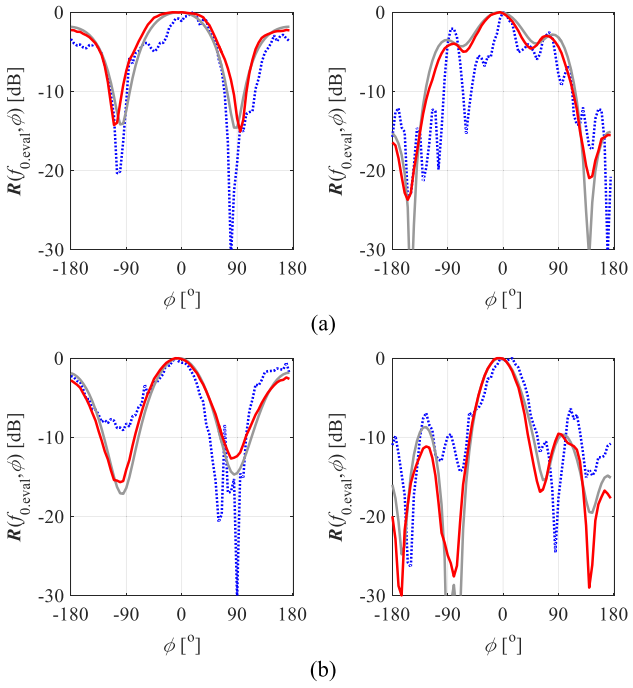

Fig. 18. Corrected (red), EM-based reference (gray), and uncorrected (blue) radiation patterns obtained in the second test site for a quasi-Yagi antenna at 4 GHz (left-hand side) and 7 GHz (right-hand side) frequencies. The measurements have been performed in: (a) yz-plane and (b) xy-plane, respectively. Note that the calibration has been performed w.r.t. AC data using the Vivaldi antenna ($f_{0.cal}$ = 3 GHz; yz-plane). (For interpretation of the references to colour in this figure legend, the reader is referred to the web version of this article.)

rapid deployment of the test equipment in distinct localizations while ensuring reliability of the TGM-corrected measurements (given the availability of calibration antennas and accurate reference data).

4.5. Benchmark and discussion

The proposed TGM correction mechanism has been benchmarked against the state-of-the-art methods where the interval bounds are determined from: (i) geometrical distance between the antennas in a system [10], and (ii) analysis of the system impulse responses [7]. It is

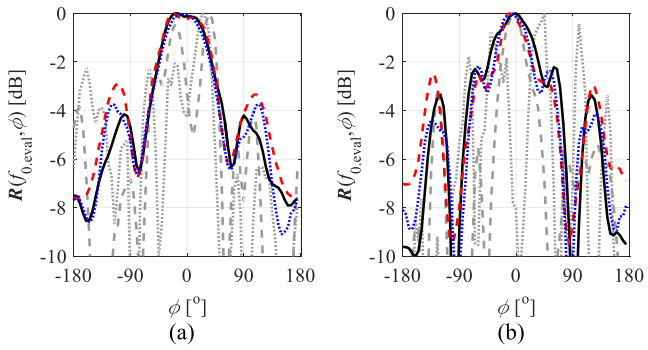

Fig. 19. Radiation patterns of the Vivaldi antenna measured in AC (—) versus characteristics obtained in the first (– –) and the second test site (●●●) at: (a) 4 GHz and (b) 5 GHz frequencies. Gray plots represent the responses obtained in the test sites before the TGM correction.

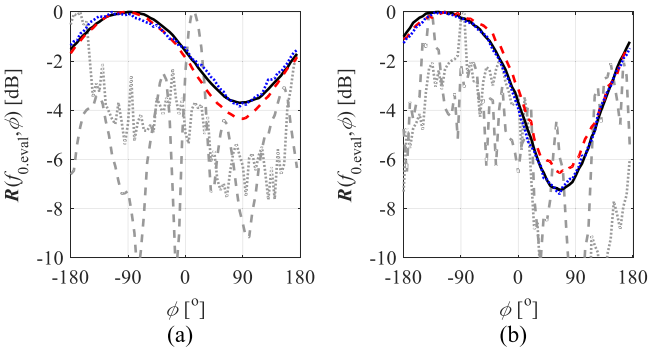

Fig. 20. Radiation patterns of the spline-based monopole measured in AC (—) versus characteristics obtained in the first (– –) and the second test site (●●●) at: (a) 4 GHz and (b) 7 GHz frequencies. Gray plots represent the responses obtained in the test sites before the TGM correction.

worth noting that the presented method has already been compared (to some extent) with the approaches from the literature (cf. Sections 4.1 and 4.2). However, the considered case studies concerned only validation of the calibration algorithm, and hence common values of the remaining TGM parameters were used for all of the methods (i.e., $B \geq c/(3\bullet D)$, $K = 201$, $N = 2^{\log2(\lceil K\rceil)+3}$). Here, performance of the proposed framework is benchmarked against specific implementations of the techniques reported in [7] and [10], respectively.

The setup of the presented method is the same as described in Section 4. The settings of benchmark techniques follow their respective guidelines summarized in Section 3.3, i.e., $B = 5\bullet c/(\delta_{n2} - \delta_{n1})$, where $\delta_{n1} = 2.1$ m and $\delta_{n2} = 2.97$ m (cf. Fig. 2) for (i), and $B = 3/(t_{i2} - t_{i1})$, with t_{i1}, t_{i2} estimated from (4) for (ii), respectively. In both cases, $N = 2^{\log2(\lceil K\rceil)+3}$ and $K = 2001$. It should be noted that specific rules concerning determination of N are not provided in [7,10], whereas the general recommendation on K is to provide large number of points (and hence, small $\partial\omega$).

The tests have been performed in the first test site (cf. Section 2) using the Vivaldi structure and spline monopole. The frequencies of interest and angular resolution have been set to $\boldsymbol{f}_0 = [4\ 6\ 8\ 10]^T$ GHz and 5°, respectively. The accuracy of the considered techniques is quantified using the RMSE (calculated w.r.t. AC measurements and averaged over $\boldsymbol{f}_0$). The results shown in Table 2 indicate that, for the considered antennas, the proposed approach offers both improved accuracy and up to almost fourfold lower cost (expressed in terms of the time expenditure required for gathering the measurement data) compared to the state-of-the-art techniques. At the same time, the method simplifies (and quantifies) determination of B and K parameters, while streamlining the identification of the TGW interval bounds using the proposed heuristic

Table 1
TGM with automatic calibration: correction performance in non-anechoic test sites.

Vivaldi antenna					Spline-based monopole				
	$f_{0.eval}$ [GHz]	3	4	Average		$f_{0.eval}$ [GHz]	4	7	Average
TS_1 [#]	$e_{R.1}$ [$] [dB]	–14.10	–13.01	–13.56	TS_1 [#]	$e_{R.1}$ [$] [dB]	–9.40	–13.43	–11.42
	$e_{R.2}$ [$] [dB]	–24.16	–19.71	–21.94		$e_{R.2}$ [$] [dB]	–31.96	–30.50	–31.23
TS_2 [#]	$e_{R.1}$ [$] [dB]	–12.30	–10.34	–11.32	TS_2 [#]	$e_{R.1}$ [$] [dB]	–11.92	–11.08	–11.50
	$e_{R.2}$ [$] [dB]	–26.98	–21.89	–24.43		$e_{R.2}$ [$] [dB]	–35.11	–36.49	–35.80

[#] TS_1 and TS_2 refer to the first and second test site (cf. Fig. 2);
[$] $e_{R.1}$ and $e_{R.2}$ denote RMSE obtained w.r.t. AC-measurements before and after TGM correction.

Table 2
Benchmark of the proposed framework against the state-of-the-art methods.

Method	Vivaldi antenna [12]					Monopole antenna [13]				
	B [GHz]	t_{n1} [ns]	t_{n2} [ns]	e_R [dB]	Cost[$] [min]	B [GHz]	t_{n1} [ns]	t_{n2} [ns]	e_R [dB]	Cost[$] [min]
(i)[!]	0.7	7.1	14.3	–15.7	40.8	0.7	7.1	14.3	–14.7	40.8
(i)[*]	1.7	7.1	10.0	–20.2	40.9	1.7	7.1	10.0	–16.3	40.9
(ii)[&]	1.5	0	15.6	–16.5	40.9	4.5	0	7.6	–8.90	41.7
(ii)[#]	1.5	0	8.8	–20.9	10.9	4.5	0	8.3	–19.2	41.7
Proposed	1.0	2.0	13.0	–23.1	10.7	3.0	6.3	8.7	–21.0	10.7

[!] The reflected signal path measured as 4.15 m (reflection from the whiteboard; see Figs. 2 and 15).
[*] The reflected signal path measured as 2.97 m (reflection from the ceiling lamps; see Figs. 2 and 15).
[&] Parameter t_{n2} calculated as max($\boldsymbol{t}_{ang}$); see Section 3.3;
[#] Parameter t_{n2} refined based on visual inspection of the impulse response;
[$] Expressed as the cost of gathering the data around the frequencies of interest with the assumed K.

method. It should be emphasized that the performance of benchmark methods is poor. The obtained RMSE values are especially high for the spline structure which demonstrates limited applicability of conventional methods for correction of its responses. Slightly better results have been obtained for the Vivaldi antenna which is due to its larger dimensions and higher gain. Furthermore, competitive accuracy of (ii) w.r.t. the proposed method has been obtained only after manual tuning of the t_{n2} parameter (cf. Section 4.2).

The presented results demonstrate usefulness of the proposed TGM framework for conducting low-cost and reasonably accurate far-field measurements of electrically small antennas in non-anechoic environments. On the other hand, due to lack of mechanisms for attenuation and/or shielding of EM radiation from the external sources, the performance of the presented method may vary depending on the center frequency of interest. For instance, the spectrum around e.g., 2.45 GHz, 5.3 GHz, or 5.8 GHz frequencies is extensively utilized by wireless communication systems. Measurements of antenna patterns in such conditions would cause deterioration of the signal-to-noise ratio on the RA-AUT path and, consequently, degrade the accuracy of TGM-corrected characteristics. Although the problem could be alleviated (to some extent) though amplification of the RA antenna signal around the affected frequencies, its investigation exceeds the scope of the work.

Another challenge associated with lack of test site shielding involves dynamic changes of propagation conditions on the RA-AUT path. Having in mind that the radiation pattern response is reconstructed from a series of data points obtained around the frequency of interest (one needs to perform 72 measurements to generate a 360° pattern in a single plane with a 5° resolution), temporal dynamics of the external EM noise may result in deterioration of its fidelity. The latter is manifested in the form of local, low amplitude distortions of the extracted characteristics that are noticeable for low-gain (e.g., electrically small, and/or omnidirectional) structures. Fig. 21 provides a conceptual illustration of the effect for the compact spline-monopole measured in the second test site. To some extent, the phenomena can be attributed to the aliasing as the presented framework exploits relatively low number of frequency samples for refinement of the measurement data [7,9,10]. Notwithstanding, the results of Fig. 22 suggest that contribution of the external noise to the distortion of TGM-corrected radiation patterns is around an order of

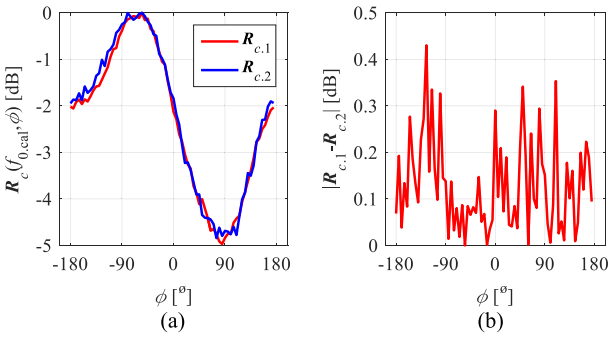

Fig. 21. TGM-corrected radiation pattern obtained for the spline-monopole antenna: (a) two measurements $\boldsymbol{R}_{c.1}$ and $\boldsymbol{R}_{c.2}$ performed around 15 min apart and (b) discrepancy between the characteristics. The results have been obtained in the second test site.

magnitude higher as compared to the aliasing-induced effects. As mentioned above, the discussed problems can be mitigated through amplification of the signal in the RA-AUT path. External noise could also be reduced by means of averaging the results from several measurements. Nonetheless, this would negatively affect the cost of the proposed procedure.

The effect of changing measurement conditions on overall correction performance can be quantized using uncertainty budget [5]. Although its detailed analysis is beyond the scope of the manuscript, a limited series of tests has been performed in the second test-site for the same setup as the one of Fig. 21. The considered experiments include repeatability of (i) measurements (performed in 15-minute intervals) corrected using the presented method (i.e., $\boldsymbol{R}(f_{0.cal})$), (ii) calibration performance under angular misalignment of CA and AUT, (iii) mechanical RF connection to the antenna, (iv) VNA calibration, and (v) transmission under folding of RF cables [5]. The distribution for all of the mentioned components but the (rectangular) angular discrepancy is Gaussian [5]. The combined uncertainty u_c for the considered factors can be expressed as [5,38]:

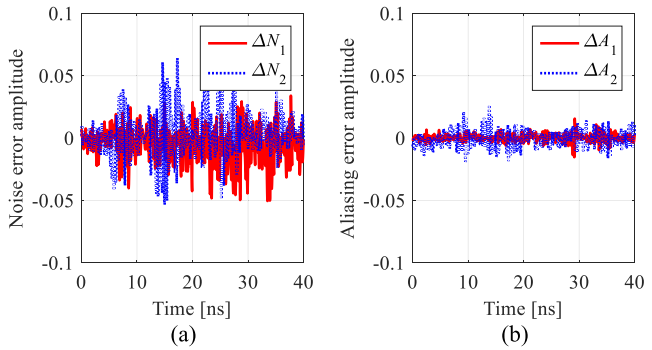

Fig. 22. Spline-monopole: impulse response errors obtained in the second test site at $\phi_a = 0°$ that result from: (a) dynamically changing external noise and (b) aliasing. The plots are obtained from a set of three measurements performed using 201, 401, and 801 points ($B = 3$ GHz). The parameter ΔN_1 represents the change of the normalized impulse responses from the 1st and 2nd (reduced to 201 points) measurement, whereas ΔA_1 denotes difference between the 2nd response represented using $K = 401$ and $K = 201$ points; ΔN_2 and ΔA_2 are extracted in the same manner.

$$u_c = \left(\sum_{i=1}^{I} u_i^2 \right)^{0.5} \tag{9}$$

Each of the components u_i ($i = 1, \ldots, 5$) has been calculated based on a series of five measurements (25 in total). It should be noted that the results of (i) are affected not only by the temporal dynamics of the propagation environment, but also temperature changes, uncertainties resulting from rotation of RF joints, (already discussed) aliasing, or repeatability of antenna alignment [5]. The factors of (9) calculated for the considered example are 0.429 dB, 0.028 dB, 0.006 dB, 0.011 dB, and 0.232 dB for (i) to (v), respectively, whereas the combined uncertainty amounts to 0.489 dB. As expected based on previous considerations, changing propagation conditions have the greatest contribution to the u_c coefficient. Moreover, a relatively large uncertainty of (v) stems from the nature of the experiment, which involved measurements using both the straightened cable and a tight loop around the cylinder with 1.5 cm radius.

It should be reiterated that the main assumption behind the proposed TGM calibration algorithm is availability of the CS along with the accurate reference data (either in the form of the high-fidelity EM simulations, or AC measurements). The algorithm does not embed mechanisms for assessing accuracy of the existing calibration data. However, identification of a very narrow interval or poor quality of the radiation patterns obtained for the CS—in a frequency band that is not heavily obstructed by other systems—might suggest insufficient fidelity of the reference information. To confirm/contradict the latter, one can re-set the algorithm with the increased number of calibration frequencies which allows for determination of less aggressive intervals. Lack of performance improvement in such a scenario would be a clear indication of inaccurate reference data.

Regardless of the above-discussed shortcomings, the presented framework supports straightforward and streamlined correction of measurements performed in unshielded, non-anechoic environments. In contrary to the state-of-the-art methods, it does not involve manual or semi-manual adjustment of the TGM interval bounds. It should be emphasized that, to the best knowledge of the authors, the problem concerning accurate TGM-enhanced measurements of electrically small antennas has not been considered in the literature. Furthermore, the experimental results indicate that resemblance between the refined measurements conducted in two different test sites is acceptable (bearing the propagation conditions). The proposed approach seem to be of particular interest for applications where the ability to perform low-cost (in terms of the required facilities and time expenditure) and rapid (including deployment the equipment) measurements of prototype microwave antennas is deemed important.

5. Conclusions

In this work, a framework for accurate radiation pattern measurements in non-anechoic environments with automatic identification of TGM interval bounds has been proposed. The method involves measurement of the so-called calibration structure (for which accurate AC-based data, or high-fidelity EM simulations are known) followed by heuristic-based optimization of the time-gating window interval. The tuning process is oriented towards a curve fitting of the on-site measurements to the reference responses. The presented technique has been validated using four electrically small radiators and benchmarked against TGM-based methods from the literature. Usefulness of the proposed framework for automatic calibration of different test sites, as well as analyses of the effects of external noise and the aliasing (resulting from utilization of relatively small number of frequency points for measurements correction) on correction performance have also been performed and further enhanced by studies concerning measurements uncertainty. The obtained results indicate that the proposed approach not only streamline configuration of the test sites for non-anechoic measurements, but also generates acceptably accurate radiation patterns at a low cost (expressed in the time required to gather data necessary for TGM-based post-processing). Furthermore, it has been demonstrated that for a given setup (e.g., test site, or particular localization of the equipment), the calibration data obtained for one antenna can be re-used to correct responses of other radiators with comparable aperture sizes.

Future work will focus on more detailed quantization of the external noise effects on the accuracy of TGM-based measurements, as well as improving reliability of the approach in the presence of (relatively) high amplitude noise. Feasibility studies concerning development of self-calibration mechanisms that do not rely on the reference measurements/EM simulations for determination of TGM interval bounds will also be performed. Self-calibration is considered important for introduction of hybrid methods that would combine time-domain measurements with alternative techniques in order to further increase reliability and fidelity of measurements in non-anechoic test sites.

CRediT authorship contribution statement

Adrian Bekasiewicz: Conceptualization, Methodology, Software, Validation, Formal analysis, Data curation, Writing – original draft, Writing – review & editing, Visualization, Supervision, Funding acquisition. **Slawomir Koziel:** Investigation, Funding acquisition. **Michal Czyz:** Investigation.

Declaration of Competing Interest

The authors declare that they have no known competing financial interests or personal relationships that could have appeared to influence the work reported in this paper.

Data availability

Data will be made available on request.

Acknowledgement

This work was supported in part by the National Science Center of Poland Grants 2020/37/B/ST7/01448, 2021/43/B/ST7/01856, National Center for Research and Development of Poland Grant NOR/POLNOR/HAPADS/0049/2019-00, as well as Gdansk University of Technology (Excellence Initiative) Grant 4/RADIUM/2021.

References

[1] G. Kim, S. Kim, Design and analysis of dual polarized broadband microstrip patch antenna for 5G mmWave antenna module on FR4 substrate, IEEE Access 9 (2021) 64306–64316.

[2] J.-W. Kim, J.-I. Oh, S.H. Han, W.-Y. Song, S.-C. Chae, J.-W. Yu, Wideband circularly polarized antenna with reconfigurable 2-dimensional axial ratio beamwidth, IEEE Access 9 (2021) 79927–79935.

[3] L. Hemming, Electromagnetic Anechoic Chambers: a fundamental Design and Specification Guide, IEEE Press, Piscataway, 2002.

[4] R. De Leo, V.M. Primiani, Radiated immunity tests: reverberation chamber versus anechoic chamber results, IEEE Trans. Instrumentation Meas. 55 (4) (2006) 1169–1174.

[5] S. Kurokawa, M. Hirose, K. Komiyama, Measurement and uncertainty analysis of free-space antenna factors of a log-periodic antenna using time-domain techniques, IEEE Trans. Instrumentation Meas. 58 (4) (April 2009) 1120–1125.

[6] V. Molina-Lopez, M. Botello-Perez, I. Garcia-Ruiz, Validation of the open-area antenna calibration site at CENAM, IEEE Trans. Instrumentation Meas. 58 (4) (2009) 1126–1134.

[7] A. Soltane, G. Andrieu, E. Perrin, C. Decroze, A. Reineix, Antenna radiation pattern measurement in a reverberating enclosure using the time-gating technique, IEEE Ant. Wireless Prop. Lett. 19 (1) (2020) 183–187.

[8] V. Fiumara, A. Fusco, G. Iadarola, V. Matta, I.M. Pinto, Free-space antenna pattern retrieval in nonideal reverberation chambers, IEEE Trans. EM Comp. 58 (3) (2016) 673–677.

[9] P, Piasecki, J, Strycharz, "Measurement of an omnidirectional antenna pattern in an anechoic chamber and an office room with and without time domain signal processing," Signal Proc. Symp., pp. 1-4, Debe, Poland, 2015.

[10] S. Loredo, M.R. Pino, F. Las-Heras, T.K. Sarkar, Echo identification and cancellation techniques for antenna measurement in non-anechoic test sites, IEEE Ant. Prop. Mag. 46 (1) (2004) 100–107.

[11] J, Mroczka, "The cognitive process in metrology," *Measurement*, vol. 46, pp. 2896–2907, 2013.

[12] J. Bai, S. Shi, D.W. Prather, Modified compact antipodal vivaldi antenna for 4–50-GHz UWB application, IEEE Trans. Microwave Theory Tech. 59 (4) (2011) 1051–1057.

[13] A. Bekasiewicz, S. Koziel, P. Plotka, K. Zwolski, EM-driven multi-objective optimization of a generic monopole antenna by means of a nested trust-region algorithm, Applied Sciences 11 (9) (2021) 3958.

[14] M. Czyz, J. Olencki, A. Bekasiewicz, A compact spline-enhanced monopole antenna for broadband/multi-band and beyond UWB applications, Int. J. Electronics Telecom. (2022).

[15] B.Y. Toh, R. Cahill, V.F. Fusco, Understanding and measuring circular polarization, IEEE Trans. Education 46 (3) (2003) 313–318.

[16] G. Leon, S. Loredo, S. Zapatero, F. Las-Heras, Radiation pattern retrieval in non-anechoic chambers using the matrix pencil algorithm, Prog. EM. Res. Lett. 9 (2009) 119–127.

[17] Z. Du, J.I. Moon, S.-S. Oh, J. Koh, T.K. Sarkar, Generation of free space radiation patterns from non-anechoic measurements using Chebyshev polynomials, IEEE Trans. Ant. Prop. 58 (8) (2010) 2785–2790.

[18] D.A. Leatherwood, E.B. Joy, Plane wave, pattern subtraction, range compensation, IEEE Trans. Ant. Prop. 49 (12) (2001) 1843–1851.

[19] B. Fourestie, Z. Altman, Gabor schemes for analyzing antenna measurements, IEEE Trans. Ant. Prop. 49 (9) (2001) 1245–1253.

[20] B. Fourestie, Z. Altman, J. Wiart, A. Azoulay, On the use of the matrix-pencil method to correlate measurements at different test sites, IEEE Trans. Ant. Prop. 47 (10) (1999) 1569–1573.

[21] E.N. Clouston, P.A. Langsford, S. Evans, Measurement of anechoic chamber reflections by time-domain techniques, IEE Proc. 135 (2) (1988) 93–97.

[22] S. Loredo, G. Leon, S. Zapatero, F. Las-Heras, Measurement of low-gain antennas in non-anechoic test sites through wideband channel characterization and echo cancellation, IEEE Ant. Prop. Mag. 51 (1) (2009) 128–135.

[23] MS2038C, Anritsu Corp., 5-1-1 Onna, Atsugi-shi, Kanagawa 243-8555, Japan.

[24] SMA connector 32K101-400L5, Rosenberger Hochfrequenztechnik GmbH & Co. KG, PO Box 1260, 84526 Tittmoning, Germany.

[25] Laminate RO4360G2, Rogers Corporation, 2225 W. Chandler Blvd., Chandler, AZ 85224, USA.

[26] Laminate RO4003C, Rogers Corporation, 2225 W. Chandler Blvd., Chandler, AZ 85224, USA.

[27] C.A. Balanis, Antenna theory analysis and design, 3rd ed., John Wiley & Sons, Hoboken, 2005.

[28] A.V. Oppenheim, R.W. Schafer, Discrete-Time Signal Processing, 3rd ed., Prentice Hall, 2009.

[29] S. Luo, Z. Chen, Iterative methods for extracting causal time-domain parameters, IEEE Trans. Microwave Theory Tech. 53 (3) (2005) 969–976.

[30] A. Morales, S.S. Agili, T. Meklachi, *S*-parameter sampling in the frequency domain and its time-domain response, IEEE Trans. Instrumentation Meas. 70 (2021) 1–13.

[31] S. Koziel, A. Bekasiewicz, "Constrained optimization for generating gain-bandwidth design trade-offs of wideband unidirectional antennas", *IET Microwaves*, Ant. Prop. 13 (7) (2019) 1017–1022.

[32] SMA connector 142-0701-201, Cinch Connectivity Solutions, 1700 Finley Road Lombard, IL 60148 USA.

[33] T.A. Milligan, Modern Antenna Design, 2nd ed., Wiley-Interscience, Hoboken, 2005.

[34] D.W, Hess, "Historical background on the use of equivalent stray signal in comparison of antenna patterns," Proc. European Conf. Ant. Prop., pp. 2522-2526, Rome, Italy, 2011.

[35] N. Munic, M. Nikolic Stevanovic, A. Djordjevic, A. Kovacevic, Evaluation of radiating-source parameters by measurements in Faraday cages and sparse processing, Measurement 104 (2017) 105–116.

[36] J, Hejselbaek, Y, Ji, Y., W, Fan, G.F, Pedersen, "Channel sounding system for mm-wave bands and characterization of indoor propagation at 28 GHz," *Int. J. Wireless Inf. Networks*, vol. 24, pp. 204-216, 2017.

[37] C.U. Bas, et al., A real-time millimeter-wave phased array MIMO channel sounder, IEEE Vehicular Techn. Conf. (2017) 1–6.

[38] G. Taraldsen, T. Berge, F. Haukland, Uncertainty of decibel levels, J. Acoustic Soc. America 138 (3) (2015) 264–269.

[39] E.R. Hunter, T. Stander, A compact, low-cost millimetre-wave anechoic chamber, European Conf. Ant. Prop, Davos, Switzerland, 2016, pp. 1–5.

[40] D, Green, D, Smith, "Design, construction and performance of a small, low cost anechoic measuring system for research applications," IEEE Ant. Prop. Soc. Int. Symp., vol. 4, pp. 1738-1741, Newport Beach, USA, 1995.